Linear Stability Investigations of Flow Over Yawed Anisotropic Compliant Walls

Marcus Zengl and Ulrich Rist

Abstract Linear stability investigations are presented for flows over anisotropic compliant walls. Hereby, a surface-based anisotropic model is incorporated, featuring stiffeners making an angle to the surface plane as well as an angle to the plane which is wall-normal and in flow direction. Results are shown for Blasius flow using compliant-wall parameters found in literature, demonstrating the effect of the yawing angle on linear stability. It is concluded that the propagation direction of the most amplified instabilities can be altered.

1 Introduction

Pavlov[5] investigated the skin properties of the dorsal fin of harbor porpoises, showing that dermal ridges—which are comparable to stiffeners of an anisotropic material—are aligned in lines making an angle to the flow direction (yawing). To investigate the effects of a yawed anisotropic compliant coating the wall model used in [1] was extended (section 2), the boundary condition incorporating this wall model was derived and validated for an Orr–Sommerfeld–Squire solver (section 3), and the effect of yawing of the material was investigated (section 4).

2 Theoretical Model of the Yawed Anisotropic Wall

The compliant wall is modeled as an elastic plate bound to a rigid base by stiff swivel arms. These arms are connected to the rigid base by springs and dampers. An illustration of the wall model is shown in figure 1. The arms make the angle θ

Marcus Zengl[1] · Ulrich Rist[2]
Institut für Aerodynamik und Gasdynamik, Universität Stuttgart, Germany
e-mail: [1]marcus.zengl@iag.uni-stuttgart.de; [2]ulrich.rist@iag.uni-stuttgart.de

to the surface plane and the yaw angle ψ to the wall-normal plane aligned with the flow direction.

The boundary condition at the wall is established by performing a Taylor series of the fluid velocities and the fluid pressure. At the location of the elongated surface the velocities and stresses of fluid and wall are matched to obtain an expression for the quantities at the wall-neutral position. Nonlinear terms of the disturbance quantities and terms in which only base-flow quantities appear are then dropped. Using the momentum equation of the wall we obtain three boundary conditions at the wall, linking the disturbance velocities and pressure. In contrast to common surface-based models found in literature, the Orr–Sommerfeld and the Squire equation are coupled by the boundary condition at the wall and must to be solved in combination.

The wall parameters can be reduced to the non-dimensional quantities

$$C_{\mathrm{m}}^{(\nu)} = \frac{\rho_{\mathrm{m}} b_{\mathrm{m}} U_\infty}{\rho \nu}; \quad C_{\mathrm{k}}^{(\nu)} = \frac{K_{\mathrm{m}} \nu}{\rho U_\infty^3}; \quad C_{\mathrm{b}}^{(\nu)} = \frac{E_{\mathrm{m}} b_{\mathrm{m}}^3 U_\infty}{12\left(1-\nu_{\mathrm{m}}^2\right)\rho \nu^3}; \quad C_{\mathrm{i}}^{(\nu)} = \frac{E_{\mathrm{m}} b_{\mathrm{m}}}{\rho \nu U_\infty}\,. \tag{1}$$

These coefficients account for the mass ratio C_{m}, spring stiffness C_{k}, flexural rigidity C_{b}, and the induced tension in the plate caused by the differential motion of the swivel arms C_{i}. The wall parameters are reflected by Young's modulus E_{m}, Poisson's ratio ν_{m}, wall density ρ_{m}, plate thickness b_{m}, and the spring stiffness K_{m}.

3 Numerical Method and Code Validation

The coupled Orr–Sommerfeld and Squire equations are solved using a shooting method. The equations are formulated as in [4] (eqn. 2.45 and 2.46). Starting from the free-stream, the system of equations is integrated using a standard 4^{th} order Runge–Kutta scheme. Linear independence of the integrated base-solutions is ensured using Godunov's orthonormalization technique described in [2]. The base solutions are added so that two of the three boundary conditions at the wall are met. To track eigenvalues, the residual ε of the third equation is then minimized using common root-finding methods starting from an initial guess. Using a technique used in [3] the eigenvalue spectrum is obtained by plotting lines of $Re(\varepsilon) = 0$ and $Im(\varepsilon) = 0$ in the complex phase-speed plane. Their intersection points are either poles or roots of the residual and are evaluated using them as initial guess of the root-finding method.

A comparison of the marginal-stability curves (for $\beta = 0$) for Blasius flow over walls with the parameters listed in table 1 is shown in figure 2. Symbols denote the results of [1]. Lines denote the results of the current method. The results are in good agreement with each other, although different formulations and numerical methods were used.

Table 1 Parameters for the cases in figure 2

case	θ	ψ	$C_{\mathrm{m}}^{(v)}$	$C_{\mathrm{k}}^{(v)}$	$C_{\mathrm{b}}^{(v)}$	$C_{\mathrm{i}}^{(v)}$
1^a	—	—	—	—	—	—
2^b	0°	0°	1.464×10^4	4.443×10^{-5}	1.208×10^{12}	—
3	60°	0°	2.211×10^3	7.405×10^{-6}	1.529×10^9	2.814×10^3
4	75°	0°	5.777×10^2	1.983×10^{-6}	2.281×10^7	6.152×10^2

[a] rigid wall case; [b] isotropic wall case

4 Results

Due to the abundance of possible wall parameters it was chosen to investigate the effect of yawing using the parameters found in [1]. These parameters have been optimized for Blasius flow using asymptotic theory. A stability diagram for case 3 ($\theta = 60^\circ$) is shown in figure 3. Lines denote marginal stability for different constant spanwise wavenumbers β, while the line for $\beta = 0$ is drawn thicker. Contours of the temporal amplification rate are shown in slices for constant streamwise wavenumbers α. The maximum amplification rate is for a wave of the spanwise wavenumber $\beta = 0$ and the diagram is symmetric w. r. t. $\beta = 0$.

Starting from the parameters in case 3 the yaw angle was modified. In figures 4, 5, and 6 the anisotropic material was yawed with the angles, $\psi = 18^\circ$, $\psi = 36^\circ$ and $\psi = 54^\circ$, respectively. For $\psi \neq 0^\circ$ the wave of the maximum amplification rate is a sideways propagating wave. The higher the yaw angle, the higher is its spanwise wavenumber. For $\beta = 0$, the unstable region is successively reduced in size and magnitude. Increasing the yaw angle, a reduction of the maximum amplification rate of the TS instability can be barely noticed. However, the Flow Induced Surface Instability (FISI) is destabilized and eventually becomes unstable for large yaw angles. Its propagation direction is in opposite direction to the TS instability, and can exhibit considerably higher amplification rates.

5 Conclusions

We have presented a viable method to study the influence of a yaw angle for anisotropic compliant walls. Increasing the yaw angle of the anisotropic material alters the propagation direction of the least stable TS waves to oblique-travelling waves and the least stable FISI towards oblique-travelling waves in the opposite spanwise direction. The maximum growth rate of TS waves is marginally reduced. However, FISI become less damped and eventually unstable.

Acknowledgements The authors gratefully acknowledge the financial support of the Deutsche Forschungsgemeinschaft (DFG) under the research grant RI680/18.

References

1. Carpenter, P.W., Morris, P.J.: The effect of anisotropic wall compliance on boundary layer stability and transition. Journal of Fluid Mechanics **218**, 171–223 (1990)
2. Conte, S.D.: The numerical solution of linear boundary value problems. SIAM Review **8**(3), 309–321 (1966). DOI 10.1137/1008063. URL http://link.aip.org/link/?SIR/8/309/1
3. Mack, L.M.: A numerical study of the temporal eigenvalue spectrum of the blasius boundary layer. Journal of Fluid Mechanics **73**(3), 497–520 (1976)
4. Mack, L.M.: Boundary-layer linear stability theory. In: Special Course on Stability and Transition of Laminar Flow, *AGARD report*, vol. 709. AGARD (1984)
5. Pavlov, V.V.: Dolphin skin as a natural anisotropic compliant wall. Bioinspiration & Biomimetics **1**(2), 31–40 (2006). DOI 10.1088/1748-3182/1/2/001

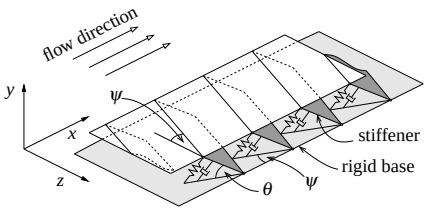

Fig. 1 Sketch of the compliant-wall model

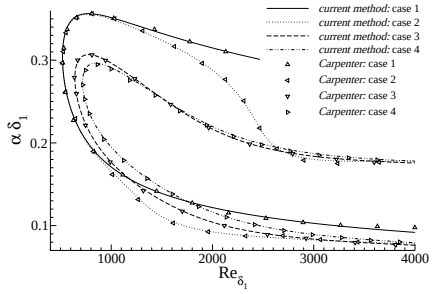

Fig. 2 Comparison of marginal-stability curves

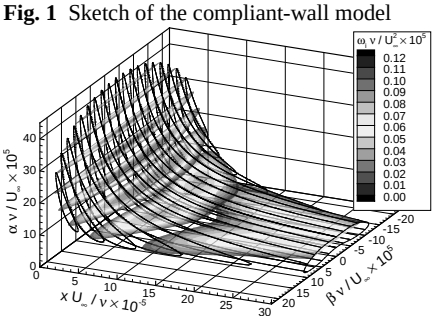

Fig. 3 Stability diagram for $\theta = 60^\circ, \psi = 0^\circ$

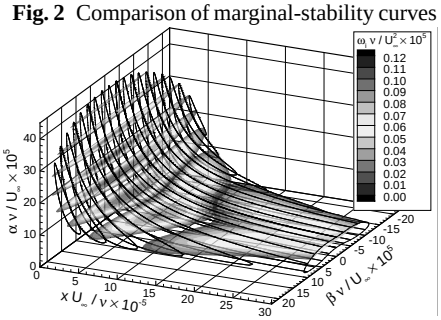

Fig. 4 Stability diagram for $\theta = 60^\circ, \psi = 18^\circ$

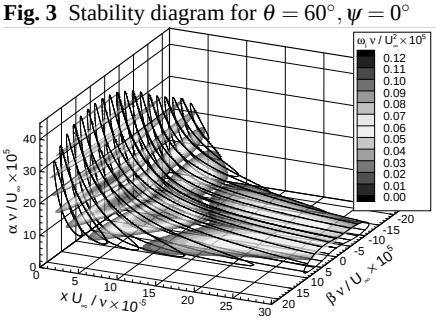

Fig. 5 Stability diagram for $\theta = 60^\circ, \psi = 36^\circ$

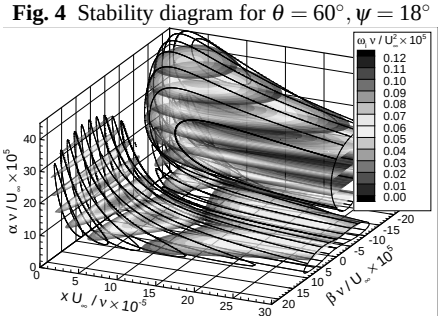

Fig. 6 Stability diagram for $\theta = 60^\circ, \psi = 54^\circ$